Longitudinal dynamics of extreme plasma-based compression of electron beams

Kelly K. Swanson,[1,*] Thamine Dalichaouch,[2] Agostino Marinelli,[1] Brendan O'Shea,[1] Mark J. Hogan,[1] and Claudio Emma[1]

[1]*SLAC National Accelerator Laboratory, Menlo Park, California, USA*
[2]*University of California, Los Angeles, Los Angeles, California, USA*

(Received 14 October 2025; accepted 19 March 2026; published 29 May 2026)

High-brightness, ultrahigh peak current electron beams are of significant interest to applications including high-energy colliders, advanced accelerator concepts, strong field quantum electrodynamics, and laboratory astrophysics. Despite such interest, compressing electron beams to attosecond pulse durations and mega-ampere peak currents while preserving beam quality remains a challenge. In this work, we examine the feasibility and challenges involved in generating such extreme beams using plasma-based compression. Using particle-in-cell and particle tracking simulations, we demonstrate that the large electric field gradients in plasma wakefields enable orders of magnitude higher compression than what can be achieved with conventional radiofrequency-based compressors. By adding energy chirps greater than 500 MeV/μm, bunch durations approaching 10 nm and peak currents approaching 1 MA can be achieved. Scalings of beam properties with respect to accelerator and plasma parameters are explored with limitations on achievable final beam duration and peak current evaluated. Optimal beam and plasma conditions are investigated for different applications, with the goal of experimentally demonstrating this technique at existing accelerator facilities. Insights gained from this study will help design the next-generation of high-brightness beams for new frontiers in scientific research.

DOI: 10.1103/ggd1-pt1y

I. INTRODUCTION

Advancements in particle accelerators have continually pushed the boundaries of disciplines including high-energy physics, attosecond science, medical physics, and materials research [1]. However, future accelerators must achieve unprecedented beam parameters to meet the demands of the next generation of applications [2–6]. High beam density, enabled by short durations and high peak currents, is critical for many of these applications.

The generation of dense electron bunches directly from a source is challenging due to detrimental collective effects, such as space-charge forces, which degrade beam quality through increased bunch emittance and energy spread [7]. To mitigate these effects, long (millimeter-scale), low-current bunches are often first created at the source and then compressed downstream in stages to produce the desired short (micrometer-scale), high-current bunches. Various compression techniques have been proposed and demonstrated, many of which rely on a time-energy correlation, or chirp, along the bunch which evolves as it propagates through a dispersive element to reshape the bunch's longitudinal phase space. Magnetic chicanes are commonly used to compress chirped, relativistic bunches via an energy-dependent path length difference. If the chirp is such that the electrons at the head of the bunch have a lower energy than those at the tail, the bunch will compress as it propagates through the chicane, with a larger chirp enabling more compression.

In many conventional accelerators, electron bunches are chirped using radiofrequency (rf) accelerator cavities, accelerating them off the peak of the electromagnetic field. A higher rf amplitude and frequency result in a larger chirp, with chirps on the order of 100 MeV/mm consistently demonstrated, compressing bunches with peak currents of 10–100 kA and durations down to ∼1 μm. However, the scalability of this approach is limited by cavity constraints, such as rf breakdown at higher voltages [8], as well as collective effects, such as coherent synchrotron radiation (CSR), which compromise the beam quality in the chicane [9,10]. Alternative techniques based on terahertz-driven structures [11,12] and the use of laser pulses [13–15] have been investigated as solutions but come with their own challenges: terahertz cavities can currently only be operated with lower bunch energies because of the low energy conversion to the THz field while optical lasers are limited

*Contact author: kswan@slac.stanford.edu

Published by the American Physical Society under the terms of the Creative Commons Attribution 4.0 International license. Further distribution of this work must maintain attribution to the author(s) and the published article's title, journal citation, and DOI.

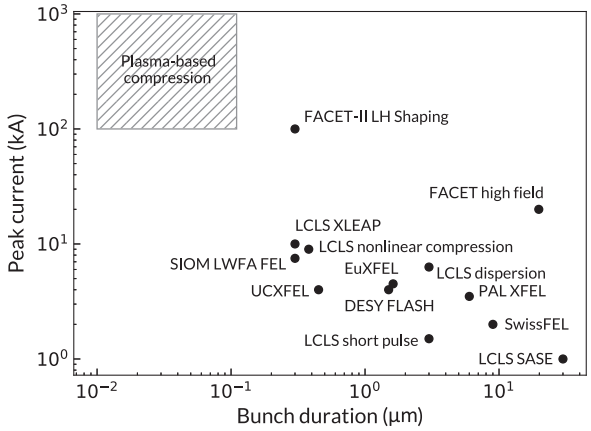


FIG. 1. Representative electron bunch parameters from accelerator facilities around the world as well as the possible bunch parameters proposed in this paper [16–28].

in the compressed peak current because only a fraction of the bunch will contribute to the current spike. The final bunch parameters achieved at various accelerator facilities worldwide using different compression methods are shown in Fig. 1.

In this paper, we discuss the design of a plasma-based compressor capable of producing electron bunches with durations approaching 10 nm and peak currents of 1 MA (see Fig. 2). This technique takes advantage of the large longitudinal electric field present in a plasma wakefield accelerator to imprint an energy chirp onto the bunch, with chirps on the order of 0.1–1 GeV/μm possible [3,29,30]. These highly chirped bunches are then focused and compressed in a magnetic chicane. Start-to-end simulations demonstrate that this technique can be incorporated into existing facilities for further compression of electron bunches by several orders of magnitude.

The paper is structured as follows: Sec. II describes the plasma chirper and provides an analytical model, benchmarked against particle-in-cell (PIC) simulations, for estimating the plasma-induced chirp based on incoming bunch and plasma parameters. Section III details compression using a postplasma chicane, studied using both numerical models and particle tracking simulations. We further investigate potential limitations of this technique in Sec. IV. While the plasma chirper can be driven by either a laser or a particle beam, our main focus is on plasma waves driven by relativistic electron bunches, although we briefly consider laser drivers in Sec. V. Future improvements aimed at addressing some of the challenges associated with implementing this technique are considered in Sec. VI.

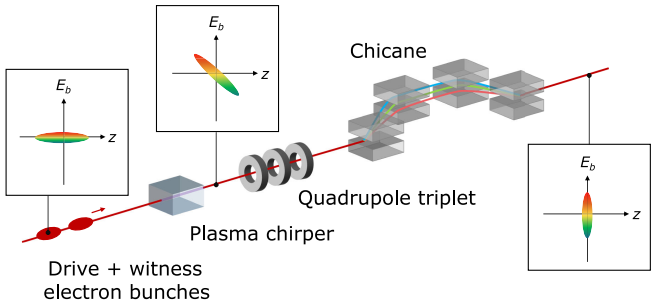


FIG. 2. Schematic layout of a plasma-based compressor and the electron bunch phase space along the beamline, where E_b is the bunch energy and z the longitudinal coordinate. Here the electron bunch is chirped in a plasma chirper driven by a preceding electron drive bunch.

II. PLASMA-BASED CHIRPER

Plasma-based accelerators are of great interest to a variety of applications due to their ability to sustain large accelerating electric fields on the order of 10–100 GV/m [31–33]. In a plasma wakefield accelerator, a particle bunch can be accelerated in the wake generated by either a laser [34] or relativistic particle beam [35] propagating through a plasma. We first consider beam-driven wakefield acceleration, where the space-charge force of an electron bunch propagating through an underdense plasma displaces the plasma electrons, driving behind it a large-amplitude wave with a relativistic phase velocity. If the bunch is sufficiently intense, it can fully expel the plasma electrons, creating behind it an ion cavity or "bubble" surrounded by a thin sheath of electrons [see Fig. 3(a)] [36]. This regime, termed the blowout or nonlinear regime, is characterized by a nearly-constant longitudinal electric field gradient in the middle of the bubble. This field can be used to introduce a chirp to a trailing witness bunch, with the head of the bunch gaining less energy than the tail. The longitudinal electric field is also transversely uniform, minimizing slice energy spread growth in the plasma. Furthermore, the focusing force within the bubble is longitudinally uniform and radially linear; therefore, the transverse emittance of each longitudinal slice of the beam can, in principle, be conserved. These features of the nonlinear regime help preserve beam quality by minimizing energy spread and emittance growth, which would otherwise degrade compression in the chicane (see Sec. IV). In the following section, we summarize an analytical model describing how the chirp of the witness bunch depends on both the plasma and drive bunch parameters.

A. Plasma wake generation

The nonlinear regime can be reached when the bunch density n_b is greater than the plasma density n_p and if the drive bunch is sufficiently small, satisfying $k_p\sigma_z \sim 1$, where σ_z is the rms bunch duration, $k_p^{-1} = c/\omega_p$, $\omega_p = \sqrt{n_p e^2/\epsilon_0 m_e}$, e is the electron charge, ϵ_0 is the vacuum permittivity, m_e is the electron mass, and c is the speed of light. In this regime, the fields inside the bubble

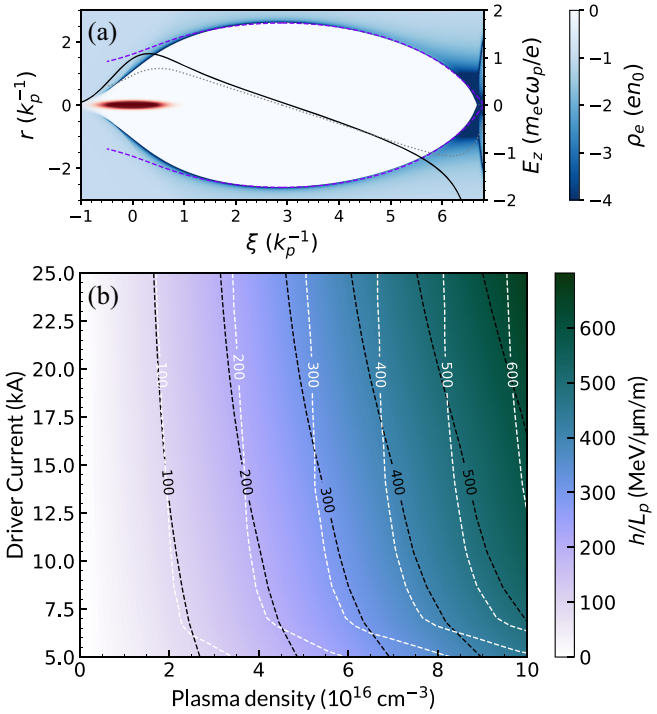


FIG. 3. (a) A representative QPAD simulation of a 10 GeV, 24 kA drive bunch (red) propagating through a plasma (blue) and driving behind it a wake in the nonlinear regime. The longitudinal electric field (black line) at the center of the bubble is linear with position ξ. Theoretical predictions of the bubble radius (purple, dashed line) and longitudinal field (gray, dotted line) well approximate the simulations. (b) The dependence of the chirp growth rate on driver current and plasma density for a 10 GeV drive bunch with 10 μm duration. The black dashed lines represent contours of constant growth rate. Growth rates calculated from the phenomenological model are presented in the white dashed lines, showing good agreement between simulations and theory over a wide parameter range.

can be determined from phenomenological models of the trajectories of the electrons that form the narrow sheath surrounding the ion cavity.

Following the single sheath model described in Ref. [37], the radius of the bubble $r_b(\xi)$ excited by a bunch with a density profile $n_b(r,\xi)$ satisfies the differential equation:

$$A(\hat{r}_b)\frac{d^2\hat{r}_b}{d(k_p\xi)^2}+B(\hat{r}_b)\hat{r}_b\left(\frac{d\hat{r}_b}{d(k_p\xi)}\right)^2+C(\hat{r}_b)\hat{r}_b=\frac{\lambda(\xi)}{\hat{r}_b}, \tag{1}$$

where $\xi=ct-z$ is the co-moving coordinate, z is the longitudinal coordinate, r is the radial coordinate, $\lambda(\xi)=\frac{k_p^2}{n_p}\int_0^{r\gg\sigma_r} rn_b(r,\xi)dr$ is the normalized current distribution of the bunch, and $\hat{r}_b=k_pr_b$ is the normalized bubble radius. The coefficients $A(\hat{r}_b)$, $B(\hat{r}_b)$, and $C(\hat{r}_b)$ depend on the bubble radius and properties of the sheath. Assuming a uniform plasma, the coefficients are given by

$$A(\hat{r}_b)=1+\left[\frac{1}{4}+\frac{\beta}{2}+\frac{1}{8}\hat{r}_b\frac{d\beta}{d\hat{r}_b}\right]\hat{r}_b{}^2, \tag{2}$$

$$B(\hat{r}_b)=\frac{1}{2}+\frac{3}{4}\beta+\frac{3}{4}\hat{r}_b\frac{d\beta}{d\hat{r}_b}+\frac{1}{8}\hat{r}_b^2\frac{d^2\beta}{d\hat{r}_b^2}, \tag{3}$$

$$C(\hat{r}_b)=\frac{1}{4}\left[1+\left(1+\frac{\beta\hat{r}_b^2}{4}\right)^{-2}\right]^{-1}, \tag{4}$$

where $\beta=\frac{(1+\alpha^2)\ln(1+\alpha)^2}{(1+\alpha)^2-1}-1$ and $\alpha=\Delta/r_b$, where Δ is the width of the sheath and can be determined empirically from PIC simulations. For a bi-Gaussian drive bunch, the maximum bubble radius R_b depends on the normalized driver current $\Lambda_d=\max\lambda(\xi)$ as

$$k_pR_b\approx 2\sqrt{\Lambda_d}, \tag{5}$$

where $\Lambda_d=n_b(k_p\sigma_r)^2/n_p=2I_d/I_A$, σ_r is the driver rms transverse spot size, I_d is the driver peak current, and $I_A=17$ kA [37].

To validate this description of the wake, a series of simulations using the PIC code QPAD were performed (see Supplemental Materials for more simulation details [38]). Figure 3(a) shows one time step from a representative simulation of a 10 GeV, 24 kA, bi-Gaussian drive bunch with 10 μm duration, 10 μm normalized emittance, and 2 μm spot size propagating through a plasma with density 5×10^{16} cm^{-3}. The corresponding theoretical prediction for the bubble radius is also shown, obtained by integrating Eq. (1) with the initial condition $R_m=r_b(\xi_m)$, where R_m is the maximum bubble radius at the longitudinal position ξ_m, and $\Delta=1.1+0.096r_b$. It can be seen that there is good agreement between theory and simulation over most of the length of the bubble.

B. Wakefield-induced chirp

The longitudinal electric field gradient $E_z'\equiv dE_z/d\xi$ at the center of the bubble is given by [37]:

$$\frac{1}{k_pE_0}\frac{dE_z}{d\xi}(\xi_m)=-\left[\frac{1}{2}+\frac{1}{2}\beta(\hat{R}_m)+\frac{1}{4}\hat{R}_m\frac{d\beta}{d\hat{r}_b}(\hat{R}_m)\right]\times\hat{R}_m^2\frac{\left[\frac{1}{4}\left(1+\frac{1}{(1+\frac{1}{4}\beta\hat{R}_m^2)^2}\right)-\frac{\lambda(\xi_m)}{\hat{R}_m^2}\right]}{1+\left[\frac{1}{4}+\frac{1}{2}\beta+\frac{1}{8}\hat{R}_m\frac{d\beta}{d\hat{r}_b}\right]\hat{R}_m^2}, \tag{6}$$

where $E_0=m_ec\omega_p/e$ and $\hat{R}_m=k_pR_m$. Figure 3(a) shows the comparison between simulations and theory of the longitudinal field. The two agree near the center of the bubble, where E_z varies linearly with longitudinal position. This region is particularly important because here the field will imprint a linear chirp on a trailing witness.

We first consider an externally injected witness (see Sec. V for other injection methods) positioned behind the driver such that it is located at the center of the bubble. As the witness propagates, it becomes chirped. If the correlated energy spread due to the chirp is significantly larger than the uncorrelated (slice) energy spread of the bunch, then the relative chirp is given by $h = \gamma^{-1} d\gamma/d\xi$, where γ is the relativistic Lorentz factor of the bunch. The change in energy after accelerating over a distance L_p is given by

$$\gamma_1 = \gamma_0 - \frac{eE_z' L_p}{m_e c^2}\xi, \tag{7}$$

where $\gamma_{0,1}$ are the relativistic Lorentz factors at the beginning and end of the plasma, respectively. Therefore, the chirp is given by

$$h = -\frac{eE_z' L_p}{\gamma_1 m_e c^2}, \tag{8}$$

where E_z' can be obtained from Eq. (6).

The chirp is sensitive to the driver current, the plasma density, and the plasma length. Because the chirp scales linearly with the plasma length, the plasma chirper can be characterized by the chirp growth rate defined as h/L_p.

A comparison between simulations and Eq. (8) demonstrates the ability to predict the chirp from the phenomenological model [see Fig. 3(b)]. Here, a 10 GeV drive bunch with 10 μm spot size, 10 μm normalized emittance, and 10 μm duration generates a bubble with a sheath width characterized by $\Delta = 1.5 + 0.01 k_p r_b$. Achieving larger chirp growth rates requires higher plasma densities and driver currents. For a 1 m-long plasma, the chirp can exceed 500 MeV/μm. The difference between simulations and theory can be attributed to a dependence of the sheath width Δ on both the driver and plasma, which are not accounted for in the comparison. Nevertheless, Eq. (8) provides a reasonable estimate of the chirp, with agreement to within 10% for driver currents exceeding 6.5 kA and plasma densities exceeding 1.5×10^{16} cm^{-3}.

For strongly driven wakes, specifically when $k_p R_b \gtrsim 4$ or $I_d/I_A \gtrsim 2$, the bubble is approximately spherical and $E_z' \simeq -m_e \omega_p^2/2e$. Beyond this threshold, in the case where there is negligible energy gain in the plasma, the magnitude of the chirp saturates to $h = \omega_p^2 L_p/2\gamma c^2$. In practice, this saturation reduces the sensitivity of the witness chirp to fluctuations in the driver peak current. In this limit, the chirp can also be expressed as $h[\mathrm{MeV/\mu m}] \simeq 90 n_p[10^{16}\,\mathrm{cm}^{-3}] L_p[\mathrm{m}]$.

III. MAGNETIC COMPRESSION

After the plasma chirper introduces a correlated energy spread to the witness bunch, a downstream dispersive element can convert this time-energy correlation into a path length difference such that particles with different energies follow different trajectories to bring them closer in time, compressing the bunch. One of the most common types of dispersive elements is a magnetic chicane [7]. We will focus on this approach as an example, specifically employing a symmetric, C-chicane with four dipole magnets, because it provides a relevant demonstration of how a plasma chirper can be integrated into existing accelerator facilities.

To analytically determine the final bunch duration and peak current after the chicane, we model the witness bunch with an initial, unchirped Gaussian distribution given by

$$f_0(z_0, \delta_0) = \frac{1}{2\pi\sigma_{z,0}\sigma_{\delta,0}} e^{-z^2/2\sigma_{z,0}^2} e^{-\delta^2/2\sigma_{\delta,0}^2}, \tag{9}$$

where z_0 is the longitudinal position, $\delta_0 = \Delta\gamma_0/\gamma_0$ is the relative energy deviation, and $\sigma_{z,0}$ and $\sigma_{\delta,0}$ are their standard deviations. Following the plasma chirper, the relative positions of the electrons z_1 remain unchanged while the energy deviation δ_1 acquires a position dependence:

$$z_1 = z_0, \tag{10a}$$

$$\delta_1 = \delta_0 + h_1 z_0 + h_2 z_0^2 + h_3 z_0^3 + O(z_0^4), \tag{10b}$$

where h_1, h_2, h_3 are the first-, second-, and third-order chirps, respectively.

The chicane modifies the longitudinal positions according to the energy deviation while leaving the energy unchanged:

$$z_2 = z_1 + R_{56}\delta_1 + T_{566}\delta_1^2 + O(\delta_1^3), \tag{11a}$$

$$\delta_2 = \delta_1, \tag{11b}$$

where R_{56} and T_{566} are the first- and second-order dispersion coefficients of the chicane. In a C-chicane, $R_{56} \simeq -2\theta^2(L_d + 2L_m/3)$, where L_m is the magnet length, L_d is the drift length between magnets, and θ is the bending angle of particles with $\delta = 0$. Higher-order terms can be written as functions of R_{56}, e.g., $T_{566} = -1.5R_{56}$ [7].

After the chicane, the final bunch duration $\sigma_{z,2}$ and current I_2 are given by

$$\sigma_{z,2}^2 = \int z_2^2 f_0[z_0(z_2, \delta_2), \delta_0(z_2, \delta_2)] d\delta_2 dz_2, \tag{12a}$$

$$I_2(z_2) = eNc \int f_0[z_0(z_2, \delta_2), \delta_0(z_2, \delta_2)] d\delta_2, \tag{12b}$$

where N is the total number of electrons.

A. Linear compression

When a witness bunch is positioned in the region of the plasma bubble where the longitudinal electric field is linear, avoiding the nonlinear region near the rear, the imprinted chirp varies linearly with position. Therefore, higher-order terms in Eq. (10b) can be neglected.

The bunch will also have an increased projected energy spread after the chirper. For small energy spreads, the electron position in the chicane depends only on its energy and the chicane R_{56}. That is, the nonlinear dependence on energy in Eq. (11a) can also be neglected. Therefore, there is a linear relationship between a particle's initial and final positions in the bunch, and the final rms bunch length is given by

$$\sigma_{z,2}^2 = (1 + hR_{56})^2\sigma_{z,0}^2 + (R_{56}\sigma_{\delta,0}\gamma_0/\gamma_2)^2. \quad (13)$$

The shortest bunch length occurs when $h = -1/R_{56}$. Assuming no significant energy gain, such that $\gamma_0 = \gamma_2$, the final bunch length simplifies to $\sigma_{z,2} = \sigma_{\delta,0}/h$. The compressed bunch duration is inversely proportional to chirp and is ultimately limited by the initial slice energy spread. For strongly driven wakes where $k_p R_b \gtrsim 4$, the compressed bunch length can be written as $\sigma_{z,2} \simeq 0.011\sigma_{\delta,0}[\mathrm{MeV}]n_p^{-1}[10^{16}\,\mathrm{cm}^{-3}]L_p^{-1}[\mathrm{m}]$.

The current is given by

$$I_2(z) = \frac{eNc}{\sqrt{2\pi}\sigma_{z,2}} e^{-z^2/2\sigma_{z,2}^2}, \quad (14)$$

where $\sigma_{z,2}$ is calculated from Eq. (12a).

B. Nonlinear compression

Nonlinear effects can accumulate in the plasma chirper or the chicane, introducing higher-order correlations between particle energy and longitudinal position in the bunch. In this case, compression will not be constant along the bunch and each longitudinal slice will compress differently. For example, at larger chirps with correspondingly larger projected energy spreads, T_{566} and higher-order dispersion coefficients in the chicane become significant.

To examine the transport of the beam from the exit of the plasma through the chicane and the effects of nonlinear compression, simulations using the particle tracking code Bmad were performed (see Supplemental Materials for more simulation details [38]). A quadrupole triplet after the plasma chirper focused the witness bunch 25 cm downstream of the final chicane dipole to an average 25 μm spot size. The triplet is followed by a C-shaped magnetic chicane. These beamline components were based on existing FACET-II infrastructure [43]. Benchmarked 1D coherent synchrotron radiation and space charge solvers in Bmad allowed for the modeling of collective effects that can affect the phase space evolution during the compression process and lead to a reduction in the final peak current.

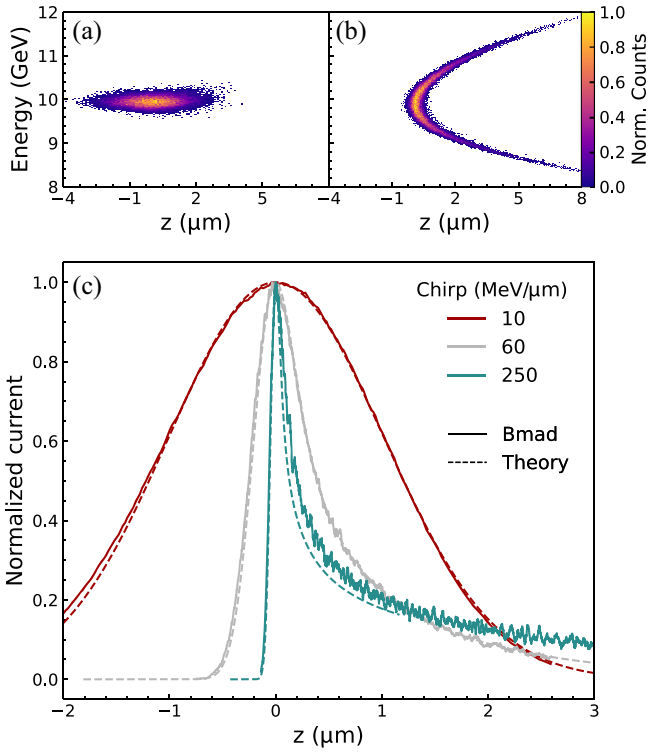


FIG. 4. Example longitudinal energy distributions after compression for bunches with 0.1% slice energy spread and chirp of (a) 10 MeV/μm and (b) 60 MeV/μm. (c) Example current profiles after compression for different chirps. Dashed lines are profiles calculated from Eq. (12), with up to third-order dispersion included in the chicane, and solid lines from simulations. In these plots, the head of the beam is on the left, and $R_{56} \approx -1/h$ and $T_{566} = -1.5R_{56}$.

Compression of 10 GeV electron bunches with 1 nC charge, 10 μm spot size, 10 μm initial duration, and 10 μm normalized emittance was simulated with varying chirp. Representative longitudinal distributions after the chicane are shown in Fig. 4. As the chirp increases, the bunch becomes shorter and develops a high-current spike followed by a long, low-current tail as a result of higher-order terms introducing a nonlinear relationship between an electron's longitudinal position and energy [see Figs. 4(a) and 4(b)]. As the magnitude of these higher-order terms increases, more charge is transferred to the tail [see Fig. 4(c)].

The compressed peak current and duration depend not only on the chirp but also on the slice energy spread (see Fig. 5). Results are shown for both the Bmad simulations and the theory presented in the previous section. Peak current begins to plateau around a chirp of 50 MeV/μm, where higher-order dispersion becomes more significant. As chirp increases, a larger fraction of the charge is located in the tail of the bunch, reducing the peak current even though the bunch duration continues to decrease. For example, for a bunch with 0.1% slice energy spread and

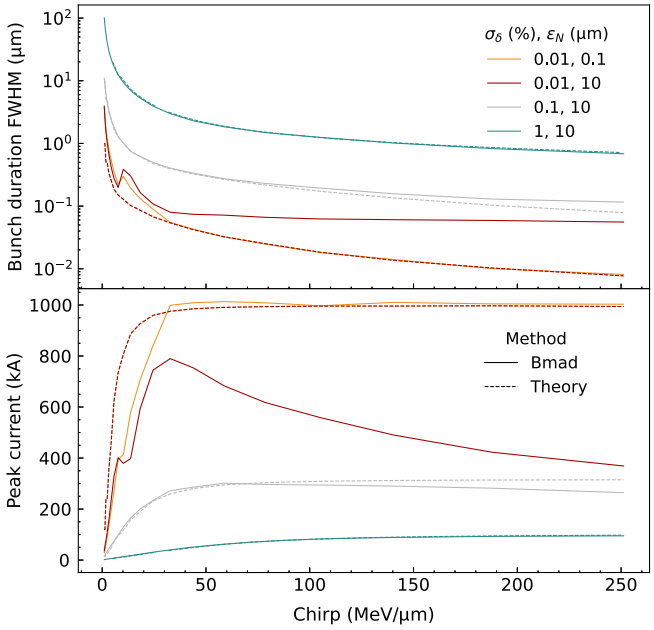


FIG. 5. Bunch duration and peak current versus chirp, with comparison between simulations (solid lines) and theory (dashed lines). Different colors correspond to different initial slice energy spreads and emittances, with smaller energy spreads and emittances resulting in shorter, higher peak current bunches.

a chirp of 50 MeV/μm, 100% of the total charge is contained within ±5 full width at half maximum (FWHM) of the current peak, compared to only 46% when the chirp is increased to 250 MeV/μm. Therefore, although chirps exceeding 500 MeV/μm can be imprinted in the plasma, such large chirps yield diminishing returns. Higher-order magnets such as sextupoles can be added to compensate for nonlinear terms, increasing the fraction of the charge in the spike and therefore the peak current of the fully compressed bunch [44,45].

The achievable compression is further limited by the bunch's slice energy spread. Energy variation among particles within the same slice leads to path length differences through the chicane, resulting in temporal broadening at the chicane exit. This effect limits the minimum achievable bunch length. A smaller initial slice energy spread enables shorter bunch durations, highlighting the importance of preserving a low slice energy spread within the plasma chirper and during transport. Achieving sub-100 nm durations requires a low-energy-spread bunch at injection as well as suppression of detrimental beam dynamics such as betatron motion (see Sec. IV).

The simulated compressed bunches deviate from the theoretical predictions of Eq. (12) at small slice energy spreads because the analytical model neglects transverse particle motion. The angular divergence associated with the bunch's emittance leads to path length differences between the electrons during propagation. Therefore, electrons with the same energy but different transverse momenta will arrive at different longitudinal positions at the end of the chicane, increasing the final bunch duration. This emittance-induced slippage becomes more significant for shorter bunches.

Assuming no acceleration, the increase in bunch duration $\Delta\sigma_z$ after distance L is given by

$$\Delta\sigma_z = \int_0^L \left[\frac{\epsilon_N^2}{\gamma^2\sigma_r^2 + (\sigma_r')^2}\right] ds, \tag{15}$$

where $\sigma_r' = d\sigma_r/ds$ and ϵ_N is the normalized emittance. The final duration then becomes $\sigma_{z,f} = \sqrt{\sigma_{z,2}^2 + \Delta\sigma_z^2}$ [46]. For a bunch with 10 μm normalized emittance, 0.01% slice energy spread, and 250 MeV/μm chirp, this slippage contributes 80 nm to the duration for this particular quadrupole triplet and chicane transport line. This slippage explains some of the deviation from the theory. When a 0.1 μm emittance bunch is compressed, the theoretical model more accurately predicts the simulation results. For the same example as above, the slippage now contributes only 0.8 nm to the duration. We note that the effect of emittance-induced slippage can be mitigated by appropriate beam conditioning using a modified magnetic lattice [46].

The difference between theory and simulation for bunches with 0.01% slice energy spreads and chirps $h < 30$ MeV/μm is attributed to CSR-induced distortions of the longitudinal phase space (see Sec. IV). However, for bunches with larger chirps and small emittances, the impact of CSR is reduced, and the theory accurately predicts the compressed bunch properties.

Because compression becomes increasingly nonlinear at large chirps, this technique also becomes less sensitive to fluctuations in plasma and beam parameters. For example, for strongly driven wakes with negligible beamloading, the chirp scales as $h \propto n_p/\gamma$. Therefore, a 1% change in either n_p or γ produces a 1% change in the chirp, where variations in γ may arise from fluctuations in the incoming beam energy or in the driver-witness separation. In addition, as shown in Fig. 3, a 10% change in driver current leads to less than a 5% change in chirp over the parameter ranges considered.

However, because the bunch duration and peak current saturate at large chirps, the compressed beam properties become increasingly insensitive to the chirp. At a chirp of 100 MeV/μm, for a bunch with 0.1% slice energy spread and 10 μm emittance, a 5% change in chirp results in a 0.1% change in peak current and 3.4% change in bunch duration. For a higher quality bunch (0.01% slice energy spread and 0.1 μm emittance), the same chirp variation results in a 0.2% change in peak current and 6.4% change in bunch duration. This tolerance to fluctuations demonstrates that plasma-based compression can be experimentally implemented without requiring prohibitively tight stability constraints.

Reaching extreme beams approaching 10 nm durations and >1 MA peak currents demands high-charge, high-quality bunches at the entrance of the chicane. Submicron emittances and low slice energy spreads are required. While achieving this bunch quality is challenging using electrons injected into the chirper from a photocathode, plasma injectors have shown promise (see Sec. V).

IV. PRACTICAL LIMITATIONS OF BUNCH COMPRESSION

While plasma-based compression is a promising approach for generating ultrashort, high-peak-current bunches, several limitations must be considered, including those related to experimental implementation and beam quality preservation. This section discusses the primary limitations and implications for the practical realization of plasma-based compression.

A. Beam loading

When a witness bunch with normalized current Λ_w is loaded into the wake, the bubble structure becomes modified due to beam loading [see Fig. 6(a) for a 10 GeV drive bunch with 24 kA peak current, 10 μm bunch duration, 10 μm normalized emittance, and 2 μm spot size followed by a similar witness bunch with 18 kA peak current propagating through a plasma with density 5×10^{16} cm^{-3}] [37,47,48]. This effect reduces the field gradient and therefore the induced chirp.

The dependence of the chirp growth rate on plasma density and witness current, including the effects of beam loading, is shown in Fig. 6(b) for a 10 GeV drive bunch with 24 kA peak current, 10 μm bunch duration, 10 μm normalized emittance, and 10 μm spot size, followed by a similar witness bunch with variable peak current. The beam loading limit is defined as the witness current for which $h/L_p = 0$, corresponding to the condition $E_z' = 0$ in Eq. (6). Solving for this limit provides the theoretical maximum witness current. Figure 6(b) demonstrates the agreement between the theory and simulations. As the witness peak current increases, the chirp growth rate decreases until it becomes negative, indicating overloading of the wake. The chirp growth rate increases linearly with witness current, and higher plasma densities allow for larger witness currents before the beam loading limit is reached.

The maximum witness current can also be estimated by comparing the space-charge force of the witness bunch to the transverse focusing force from the wakefield [37]:

$$\Lambda_{w,\max} = \frac{(k_p R_b)^2}{3.2}, \tag{16}$$

where the factor of 3.2 was determined from simulations. As the bubble radius increases, it can support higher witness currents. Theoretical predictions for $k_p R_b$ can be determined from Eq. (1), and this scaling is compared to simulations in Fig. 6(b). For a short $(k_p \sigma_z \sim 1)$ bi-Gaussian drive bunch, the maximum bubble radius scales as $k_p R_b = 2\sqrt{\Lambda_d}$. Therefore, the maximum witness current is proportional to the driver current, $\Lambda_{w,\max} \propto \Lambda_d$. A higher driver current increases the limit on witness current before beam loading suppresses the witness chirp.

For example, a wake driven by a 10 GeV, 24 kA peak current electron bunch with 10 μm spot size and duration propagating in a plasma with density 5×10^{16} cm^{-3} can chirp a trailing witness with peak current up to 17.6 kA. Increasing the plasma density to 10^{17} cm^{-3} increases the maximum witness peak current to 21.4 kA [see Fig. 6(b)].

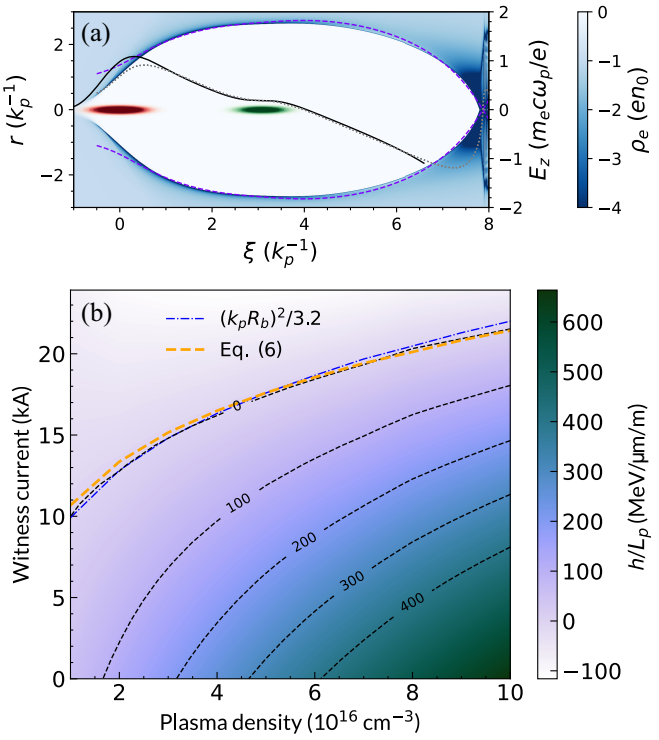


FIG. 6. (a) A representative QPAD simulation of a 10 GeV, 24 kA drive bunch with 10 μm spot size and duration (red), followed by a similar witness bunch with 18 kA peak current (green), propagating through a plasma (blue). The longitudinal electric field (black line) in the center of the wake is flattened at the location of the witness due to beam loading. Theoretical predictions of the bubble radius (purple, dashed line) and longitudinal electric field (gray, dotted line) show good agreement with the simulation, where the sheath has been defined by $\Delta = 1.1 + 0.4 r_b$. (b) The chirp growth rate h/L_p versus witness current and plasma density. The chirp growth rate is defined at the center of the witness bunch. Contours of constant chirp growth rate from simulations are shown in labeled black dashed lines. The comparison of the theoretical beam loading limit where $h/L_p = 0$ from Eq. (6) is also shown (orange, dashed line), assuming a sheath with $\Delta = 1.5 + 0.1 k_p r_b$, as well as the $(k_p R_b)^2$ scaling (blue, dashed line).

Since the witness peak current determines the magnitude of beam loading for a fixed driver and plasma, increasing the witness duration for a fixed charge helps mitigate the reduction in chirp. However, a longer bunch will also have a larger projected energy spread, leading to chromatic effects in the bunch transport downstream of the plasma. The trade-offs between these effects must be considered during the overall beamline design, with the optimal parameters depending on the application's requirements.

B. Nonlinear energy chirp

An approximately linear chirp enables the compression of the maximum charge into a high-current spike using conventional bunch compressors, without requiring additional components such as higher-order magnets. A linear chirp can be achieved either by operating in the nonlinear regime, where E_z' is constant over most of the length of the bubble or operating in the linear regime with a sufficiently short witness bunch. In the former case, the driver bunch density must be greater than the plasma density $n_b > n_p$. This condition puts an upper bound on the plasma density for a given driver density. For a 10 μm duration, 10 μm spot size driver with 2 nC of charge, this requires $n_p < 8 \times 10^{17}$ cm^{-3}. In the latter case, the nonlinear electric field in the linear regime will contribute to nonlinear components to the chirp. However, these terms are negligible compared to the linear component if the witness is short, i.e., $k_p\sigma_z \ll 1$.

Beam loading could also introduce a nonlinear chirp. For a high-current witness, the longitudinal electric field gradient within the bunch will no longer be constant, adding a nonlinear correlation between electron energy and longitudinal position. This effect could limit the extent to which the bunch can be fully compressed. However, as shown in Fig. 6(a), up to the beam loading limit, the longitudinal field remains approximately linear across the region of the bunch that contains most of the charge. The nonlinear deviations become more significant only at the head and tail of the bunch, where the charge fraction is low. Therefore, near-optimal compression can still be achieved for a high-current witness. To further increase compression, the longitudinal bunch profile can be tailored to produce a more linear energy chirp [47–49].

C. Betatron motion

The final bunch duration depends on its slice energy spread at the chicane entrance (see Fig. 5). While relative slice energy spreads can reach 10^{-5} for bunches directly from a photoinjector and on the order of 10^{-4} for relativistic electrons accelerated in an rf accelerator or a self-injected in a plasma [43,50,51], additional dynamics during propagation in the plasma can cause a detrimental increase in the slice energy spread. In particular, as the bunch propagates through the plasma, transverse dynamics can significantly contribute to this growth.

In the nonlinear regime of plasma wakefield accelerators, the focusing force scales linearly with radius, making the transverse motion of an electron depend on its initial radial position. Off-axis electrons will undergo betatron oscillations, which cause them to slip longitudinally relative to their original slice in the bunch. When the bunch is transversely matched to the plasma focusing force, it will propagate with a constant, matched spot size given by $\sigma_{r,m}^2 = \sqrt{2/\gamma}(\epsilon_N/k_p)$. In contrast, a mismatched bunch experiences oscillations in its spot size during propagation, leading to stronger longitudinal slippage and a larger slice energy spread. Without mitigation, betatron-induced slice energy spread growth can limit the compressed bunch duration.

The slice energy spread after the plasma due to betatron motion is given by [52]:

$$\frac{\sigma_{\gamma,1}}{\gamma_1} \simeq \sqrt{\frac{2em_ec^2}{\gamma_0}}\frac{\sqrt{K}E_z'}{E_z^2}(F_m\epsilon_N)\frac{(\sqrt{\Gamma}-1)^2}{\Gamma^{3/2}}, \tag{17}$$

where $\Gamma = \gamma_1/\gamma_0$, K is the focusing field strength, $F_m = [(M^4+1)/2\ M^2]^{1/2}$ is a measure of how matched the beam is to the wake, $M = \beta/\beta_m$, $\beta = \gamma_0\sigma_r^2/\epsilon_N$ is the incoming bunch beta function, and $\beta_m = \gamma_0\sigma_{r,m}^2/\epsilon_N$ is the matched beta function.

In the nonlinear regime, the focusing field scales as $K \propto m_e\omega_p^2/e$, the longitudinal electric field as $E_z \propto m_ec\omega_p/e$, and the field gradient as $E_z' \propto m_ec\omega_p^2/e$. Therefore, $\sigma_{\gamma,1}/\gamma_1 \propto \sqrt{n_p}$. For a fixed energy gain, reducing the plasma density helps preserve a small slice energy spread. However, it also weakens the electric field gradient and therefore the chirp.

For a fixed plasma density, reducing the field gradient E_z' through beam loading will also reduce the energy variation between slices and mitigate the energy spread growth due to slippage. While many applications of plasma accelerators such as colliders and free-electron lasers aim to completely flatten the accelerating field for a constant energy gain along the bunch [47,53], the plasma chirper requires a nonzero gradient to induce the chirp needed for compression.

Instead, growth in the slice energy spread can be mitigated by reducing the bunch emittance, improving the matching of the bunch spot size to the plasma wake, or using hollow plasma channels. For a 10 GeV drive and witness bunch with 10 μm spot size, 10 μm normalized emittance, 10 μm duration, and 10^{-4} initial slice energy spread propagating through a plasma with density 5×10^{16} cm^{-3} ($F_m = 29$), the witness bunch slice energy spread will grow to 1.8×10^{-3} after being accelerated to 12 GeV. Reducing the bunch spot size to its matched spot size, $\sigma_r = 1.5$ μm ($F_m = 1$) would reduce this growth by an order of magnitude.

However, achieving such tight focusing within a practical distance remains a challenge. Ongoing work aims to address this difficulty by using a longitudinally tapered density profile to facilitate matching of the bunch into the plasma [54,55].

To fully suppress slice energy spread growth, hollow plasma channels could be considered. In contrast to uniform plasmas, they have zero or negligible focusing fields inside the channel [56,57]. In this case, $K = 0$, mitigating slice energy spread due to betatron motion.

In addition to betatron-induced slippage, the impact of betatron radiation, also a byproduct of betatron motion, needs to be considered. As the electrons oscillate in the wake, they will emit synchrotron radiation, known as betatron radiation, which causes them to lose energy. Electrons with larger oscillation amplitudes will lose more energy, increasing the slice energy spread [52,58]. The energy spread due to slippage will be the major contribution if $(\gamma_0^2 e^3/15\pi c^5 m_e^2 \epsilon_0)(E_z/E_z') \ll 1$. For the bunch parameters above, slippage due to betatron motion will dominate the effects of betatron radiation up to energies of approximately 76 GeV for a plasma density of 1×10^{17} cm^{-3}. The energy at which the dominant effect transitions from betatron slippage to betatron radiation increases at lower plasma densities. Therefore, for the bunch and plasma parameters considered in this paper, the contribution to the slice energy spread due to betatron radiation is negligible.

D. Transport

After the plasma chirper, the witness bunch needs to be transported through the chicane. However, once the bunch exits the plasma, it is no longer focused by the strong fields in the wake. If there is a sharp plasma-vacuum transition, the bunch will strongly diverge in the drift section, and large focusing magnetic fields close to the plasma exit would be required to capture and transport the bunch without significant loss of charge and emittance growth [59–61].

Longitudinally tapering the density profile at the plasma exit can relax the focusing requirements. An exit density ramp gradually reduces the focusing fields in the wake, allowing the bunch size to increase such that it exits the plasma without a large divergence. This taper enables the bunch to be more easily coupled into downstream transport optics [55,62].

Focusing the bunch after the plasma can be achieved using various components, including quadrupole magnets, solenoids, or plasma lenses. While this study considers quadrupole focusing, similar principles apply to other systems. The strengths of the quadrupoles were optimized to focus the energy corresponding to the peak current in the bunch 25 cm downstream of the final chicane dipole. However, due to the chromaticity of the quadrupoles, electrons with different energies will focus at different longitudinal locations. This energy-dependent shift modifies the longitudinal phase space and therefore the chirp at the entrance of the chicane. However, for the conditions considered here, this effect is negligible. With an initial 250 MeV/μm chirp at the entrance of the quadrupole triplet, the change in chirp due to chromaticity is less than 1%, with negligible effect on bunch duration at the chicane entrance. The chromatic effects will become more significant with stronger magnets and larger projected energy spreads, but they can be mitigated if needed by using achromatic optics to compensate for chromatic aberrations [63] or by injecting a shorter bunch, which results in a smaller projected energy spread for the same chirp.

E. Coherent synchrotron radiation

Coherent synchrotron radiation can increase the energy spread and emittance of the bunch as it is compressed in the chicane. Along a bend, such as in the chicane dipole, the curved trajectory causes radiation emitted by electrons at the tail of the bunch to catch up with and interact with electrons ahead of it, leading to distortion of the bunch's longitudinal phase space.

As the tail electrons radiate, they lose energy while the electrons at the head gain energy. This CSR-induced energy spread along a bend with radius R_{bend} can be described analytically in the thin beam limit defined by $\sigma_r R_{\mathrm{bend}}^{-1/3} \sigma_z^{-2/3} \ll 1$, where the bunch can be approximated as a longitudinal line charge and transverse effects can be neglected. This approximation, which has been benchmarked with experiments [64,65], is valid for the parameters considered in this study. Therefore, for a Gaussian density profile, the rms energy spread induced by CSR is given by [9]:

$$\sigma_{\delta,\mathrm{CSR}} \approx 0.22 \frac{e^2 N}{4\pi\epsilon_0 \gamma m_e c^2} \frac{L_m}{R_{\mathrm{bend}}^{2/3} \sigma_z^{4/3}}. \tag{18}$$

As this change in energy occurs within a dispersive section, it couples into the bunch's transverse phase space, leading to beam quality degradation such as increased emittance and reduced peak current.

While higher charge and stronger compression contribute to more significant CSR-induced energy spread and emittance growth, the large chirps generated by a plasma chirper allow the use of a chicane with more gentle bends, which helps mitigate the impact of CSR. This follows from the relation $1/h = -R_{56} \simeq 2\theta^2(L_d + 2L_m/3)$, where $\theta = L_m/R_{\mathrm{bend}}$.

The impact of CSR on the bunches considered here was evaluated by comparing the energy distributions at the chicane exit with and without the CSR solver included in the Bmad simulations. As shown in Fig. 7 for a compressed 700 kA bunch with 0.01% slice energy spread, CSR induces distortions in the energy distribution at the highest-density region but has a minimal effect on the final bunch duration and current. For this example, CSR reduces the peak current by 6%.

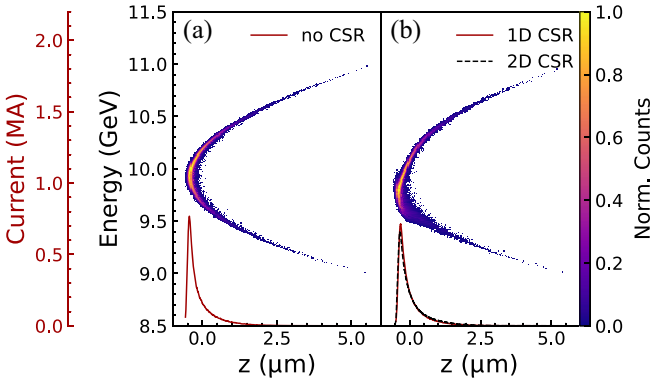


FIG. 7. Longitudinal energy and current distributions of bunches with 0.01% slice energy spread and 25 MeV/μm chirp with (a) CSR model off and (b) CSR model on. The head of the beam is on the left. Although CSR distorts the energy distribution in the highest-density region of the bunch, its effect is minimal for the bunch parameters considered here. The difference between the current distributions predicted by the 1D (red, solid line) and 2D CSR (black, dashed line) models is shown in (b), demonstrating overall good agreement between the two models.

At higher compression, the 1D CSR model may no longer be an adequate description of the beam dynamics, and CSR effects can become more noticeable. Nevertheless, the impact of CSR on the longitudinal distribution remains minimal for the parameter ranges considered here. In the case where the bunch is compressed to a peak current of 700 kA, a 2D CSR model [66] predicts a 14% decrease in peak current compared to the 1D model [see Fig. 7(b)], with the overall profile remaining largely unchanged. Therefore, although 2D CSR effects contribute more at higher compression, they do not significantly affect the main conclusions of this study.

However, if bunches are compressed to even higher peak currents, CSR will become increasingly detrimental, motivating the development of several mitigation methods, including longitudinal pulse shaping and emittance exchange [67,68]. In addition, an asymmetric S-chicane, consisting of unequal bend angles and drift lengths, has been theoretically proposed to suppress emittance growth by an order of magnitude relative to symmetric designs [69].

V. LASER DRIVERS AND PLASMA INJECTORS

Previous sections considered externally injecting an electron witness bunch into a wake generated by an electron driver. However, plasma compression is not limited to using beam-driven wakes. A high-intensity laser pulse can also drive a plasma wave, generating longitudinal electric fields that can chirp an injected electron bunch [34]. Beyond external injection, plasma-based injection is an alternative approach for generating the witness bunch. Many innovative injection mechanisms for producing high-quality bunches have been proposed and demonstrated [70–73]. In particular, plasma-based

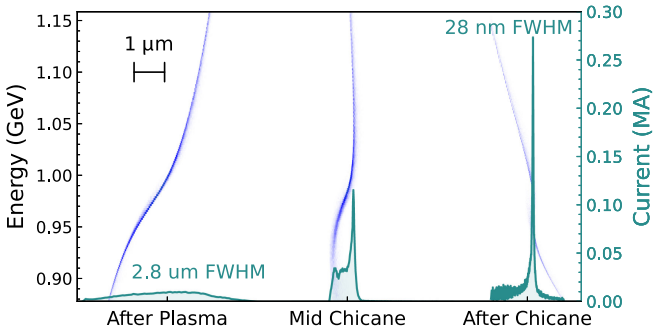


FIG. 8. Longitudinal phase space evolution from the laser-driven plasma injector to the exit of the chicane.

injectors can deliver short ($<\lambda_p$) bunches with small emittance [$\mathcal{O}$ (1 μm)] and small slice energy spreads [$\mathcal{O}$ (0.01%)], ideally suited for plasma-based compression.

To highlight the similarities and differences between the various drivers and injection mechanisms, we simulated a representative laser-driven, plasma-based compressor. The QPAD simulation of the plasma chirper assumed an injected electron bunch with 100 pC charge, 2.8 μm FWHM duration, 1 μm emittance, 100 MeV initial energy with a matched spot size of 1.1 μm. The parameters of this injected bunch were chosen as a representative example of what is reasonably achievable with existing injection methods such as density downramp injection.

In this example, a 100 TW laser pulse with 17 fs duration and 15 μm spot size propagating through a 0.7 cm plasma with density 2×10^{18} cm^{-3} accelerated the injected bunch to 1 GeV with 60 MeV/μm chirp and 0.5% final slice energy spread. After subsequent compression in a chicane, the bunch is compressed to 28 nm FWHM duration (see Fig. 8). The short initial bunch length results in a smaller projected energy spread after the plasma chirper, minimizing chromaticity during transport and higher-order compression in the chicane. Therefore, shorter bunches with higher peak currents can be produced for the same chirp. In conjunction with a small slice energy spread and emittance, a sub-100 nm duration was achieved.

VI. CONCLUSIONS

This study demonstrates the viability of plasma-based compression as an approach for generating electron beams at unprecedented peak currents and ultrashort durations. By taking advantage of the large acceleration gradient in a plasma wakefield, energy chirps several orders of magnitude greater than what is achievable using conventional methods can be imprinted onto the beam. Subsequent compression in a magnetic chicane enables the generation of nanometer-scale bunches with mega-ampere currents.

Several processes that can degrade compression were examined. Strong transverse fields in the plasma can drive slice energy spread growth. Chromaticity in the quadrupole

triplet can reduce the attainable peak current. CSR in the chicane can distort the longitudinal phase space, and beam loading in the plasma can limit the total charge. While each of these effects introduces limits on the performance of the compressor, advances in plasma density tailoring, chicane design, and beam shaping provide a path toward their mitigation. These advances would further support the practical implementation of plasma-based compression. It should be noted that this study focuses on longitudinal beam dynamics, but transverse dynamics will be examined in the future.

While this technique was demonstrated using beam- and laser-driven wakefield accelerators followed by a magnetic chicane, the approach is broadly applicable and can be realized using a variety of other chirping and compression methods. For example, dielectric wakefield accelerators can also sustain large acceleration gradients [74] while other forms of compression, such as velocity bunching or plasma-based chicanes, may be more suitable for a particular application [75,76]. These examples highlight the versatility of plasma-based compression. In addition, its compatibility with existing accelerator facilities makes near-term experimental implementation feasible. By offering a practical route to extreme electron beams, plasma-based compression opens new possibilities for accelerator-based science.

ACKNOWLEDGMENTS

We gratefully acknowledge J. Tang for their valuable contributions to the 2D CSR simulations. This work was supported by the U.S. Department of Energy under Contract No. DE-AC01-76SF00515. C. E. and K. K. S. acknowledge support from the Department of Energy Early Career Research Program.

DATA AVAILABILITY

The data that support the findings of this article are not publicly available upon publication because it is not technically feasible and/or the cost of preparing, depositing, and hosting the data would be prohibitive within the terms of this research project. The data are available from the authors upon reasonable request.

[1] A. M. Sessler and E. Wilson, *Engines of Discovery: A Century of Particle Accelerators* (World Scientific Publishing Co., Singapore, 2014).

[2] E. Adli *et al.*, HALHF: A hybrid, asymmetric, linear Higgs factory using plasma- and rf-based acceleration, arXiv:2503.19880.

[3] C. Emma, X. Xu, A. Fisher, R. Robles, J. P. MacArthur, J. Cryan, M. J. Hogan, P. Musumeci, G. White, and A. Marinelli, Terawatt attosecond x-ray source driven by a plasma accelerator, APL Photonics **6**, 076107 (2021).

[4] A. Matheron *et al.*, Probing strong-field QED in beam-plasma collisions, Commun. Phys. **6**, 141 (2023).

[5] A. Benedetti, M. Tamburini, and C. H. Keitel, Giant collimated gamma-ray flashes, Nat. Photonics **12**, 319 (2018).

[6] J. B. Rosenzweig, G. Andonian, P. Bucksbaum, M. Ferrario, S. Full, A. Fukusawa, E. Hemsing, B. Hidding, M. Hogan, P. Krejcik, P. Muggli, G. Marcus, A. Marinelli, P. Musumeci, B. O'Shea, C. Pellegrini, D. Schiller, and G. Travish, Teravolt-per-meter beam and plasma fields from low-charge femtosecond electron beams, Nucl. Instrum. Methods Phys. Res., Sect. A **653**, 98 (2011).

[7] A. W. Chao, K. H. Mess, M. Tigner, and F. Zimmermann, *Handbook of Accelerator Physics and Engineering* (World Scientific, Singapore, 2013).

[8] E. I. Simakov, V. A. Dolgashev, and S. G. Tantawi, Advances in high gradient normal conducting accelerator structures, Nucl. Instrum. Methods Phys. Res., Sect. A **907**, 221 (2018).

[9] Y. S. Derbenev, J. Rossbach, E. L. Saldin, and V. D. Shiltsev, Microbunch radiative tail—head interaction, Technical Report No. TESLA-FEL 1995-05, Deutsches Elektronen-Synchrotron DESY, 1995.

[10] H. H. Braun, R. Corsini, L. Groening, F. Zhou, A. Kabel, T. O. Raubenheimer, R. Li, and T. Limberg, Emittance growth and energy loss due to coherent synchrotron radiation in a bunch compressor, Phys. Rev. ST Accel. Beams **3**, 124402 (2000).

[11] L. Zhao, T. Jiang, C. Lu, R. Wang, Z. Wang, P. Zhu, Y. Shi, W. Song, X. Zhu, C. Jing, S. Antipov, D. Xiang, and J. Zhang, Few-femtosecond electron beam with terahertz-frequency wakefield-driven compression, Phys. Rev. Accel. Beams **21**, 082801 (2018).

[12] E. C. Snively, M. A. K. Othman, M. Kozina, B. K. Ofori-Okai, S. P. Weathersby, S. Park, X. Shen, X. J. Wang, M. C. Hoffmann, R. K. Li, and E. A. Nanni, Femtosecond compression dynamics and timing jitter suppression in a THz-driven electron bunch compressor, Phys. Rev. Lett. **124**, 054801 (2020).

[13] A. A. Zholents, Method of an enhanced self-amplified spontaneous emission for x-ray free electron lasers, Phys. Rev. ST Accel. Beams **8**, 040701 (2005).

[14] T. Tanaka, Electron bunch compression with an optical laser, Phys. Rev. Accel. Beams **22**, 110704 (2019).

[15] C. Li, W. Wang, H. Zhang, Z. Guo, X. Xu, Z. He, S. Zhang, Q. Jia, L. Wang, and D. He, Few-femtosecond MeV electron bunches for ultrafast electron diffraction, Phys. Rev. Appl. **17**, 064012 (2022).

[16] P. Emma *et al.*, First lasing and operation of an ångstrom-wavelength free-electron laser, Nat. Photonics **4**, 641 (2010).

[17] C. Behrens, F.-J. Decker, Y. Ding, V. A. Dolgashev, J. Frisch, Z. Huang, P. Krejcik, H. Loos, A. Lutman, T. J. Maxwell, J. Turner, J. Wang, M.-H. Wang, J. Welch, and J. Wu, Few-femtosecond time-resolved measurements of x-ray free-electron lasers, Nat. Commun. **5**, 3762 (2014).

[18] R. Robles and J. Rosenzweig, Compression of ultra-high brightness beams for a compact x-ray free-electron laser, Instruments **3**, 53 (2019).

[19] M. W. Guetg, A. A. Lutman, Y. Ding, T. J. Maxwell, F.-J. Decker, U. Bergmann, and Z. Huang, Generation of high-

power high-intensity short x-ray free-electron-laser pulses, Phys. Rev. Lett. **120**, 014801 (2018).

[20] L. T. Ke, K. Feng, W. T. Wang, Z. Y. Qin, C. H. Yu, Y. Wu, Y. Chen, R. Qi, Z. J. Zhang, Y. Xu, X. J. Yang, Y. X. Leng, J. S. Liu, R. X. Li, and Z. Z. Xu, Near-GeV electron beams at a few per-mille level from a laser wakefield accelerator via density-tailored plasma, Phys. Rev. Lett. **126**, 214801 (2021).

[21] S. Huang, Y. Ding, Y. Feng, E. Hemsing, Z. Huang, J. Krzywinski, A. A. Lutman, A. Marinelli, T. J. Maxwell, and D. Zhu, Generating single-spike hard x-ray pulses with nonlinear bunch compression in free-electron lasers, Phys. Rev. Lett. **119**, 154801 (2017).

[22] J. Duris *et al.*, Tunable isolated attosecond x-ray pulses with gigawatt peak power from a free-electron laser, Nat. Photonics **14**, 30 (2020).

[23] B. Schmidt, N. M. Lockmann, P. Schmüser, and S. Wesch, Benchmarking coherent radiation spectroscopy as a tool for high-resolution bunch shape reconstruction at free-electron lasers, Phys. Rev. Accel. Beams **23**, 062801 (2020).

[24] S. Corde, E. Adli, J. M. Allen, W. An, C. I. Clarke, B. Clausse, C. E. Clayton, J. P. Delahaye, J. Frederico, S. Gessner, S. Z. Green, M. J. Hogan, C. Joshi, M. Litos, W. Lu, K. A. Marsh, W. B. Mori, N. Vafaei-Najafabadi, D. Walz, and V. Yakimenko, High-field plasma acceleration in a high-ionization-potential gas, Nat. Commun. **7**, 11898 (2016).

[25] C. Emma, N. Majernik, K. Swanson, R. Ariniello, S. Gessner, R. Hessami, M. Hogan, A. Knetsch, K. Larsen, A. Marinelli, B. O'Shea, S. Perez, I. Rajkovic, R. Robles, D. Storey, and G. Yocky, Experimental generation of extreme electron beams for advanced accelerator applications, Phys. Rev. Lett. **134**, 085001 (2025).

[26] E. Prat, P. Dijkstal, M. Aiba, S. Bettoni, P. Craievich, E. Ferrari, R. Ischebeck, F. Löhl, A. Malyzhenkov, G. L. Orlandi, S. Reiche, and T. Schietinger, Generation and characterization of intense ultralow-emittance electron beams for compact x-ray free-electron lasers, Phys. Rev. Lett. **123**, 234801 (2019).

[27] H.-S. Kang *et al.*, FEL performance achieved at PAL-XFEL using a three-chicane bunch compression scheme, J. Synchrotron Radiat. **26**, 1127 (2019).

[28] N. M. Lockmann, C. Gerth, B. Schmidt, and S. Wesch, Noninvasive THz spectroscopy for bunch current profile reconstructions at MHz repetition rates, Phys. Rev. Accel. Beams **23**, 112801 (2020).

[29] R. D'Arcy *et al.*, Tunable plasma-based energy dechirper, Phys. Rev. Lett. **122**, 034801 (2019).

[30] A. Ferran Pousa, A. Martinez de la Ossa, R. Brinkmann, and R. W. Assmann, Compact multistage plasma-based accelerator design for correlated energy spread compensation, Phys. Rev. Lett. **123**, 054801 (2019).

[31] I. Blumenfeld, C. E. Clayton, F.-J. Decker, M. J. Hogan, C. Huang, R. Ischebeck, R. Iverson, C. Joshi, T. Katsouleas, N. Kirby, W. Lu, K. A. Marsh, W. B. Mori, P. Muggli, E. Oz, R. H. Siemann, D. Walz, and M. Zhou, Energy doubling of 42 GeV electrons in a metre-scale plasma wakefield accelerator, Nature (London) **445**, 741 (2007).

[32] S. Barber, F. Kohrell, C. Doss, K. Jensen, C. Berger, F. Isono, Z. Eisentraut, S. Schröder, A. Gonsalves, K. Nakamura, G. Plateau, R. van Mourik, M. Gracia-Linares, L. Labun, B. Hegelich, S. Milton, C. Geddes, J. Osterhoff, C. Schroeder, E. Esarey, and J. van Tilborg, Greater than 1000-fold gain in a free-electron laser driven by a laser-plasma accelerator with high reliability, Phys. Rev. Lett. **135**, 055001 (2025).

[33] A. Picksley, J. Stackhouse, C. Benedetti, K. Nakamura, H. E. Tsai, R. Li, B. Miao, J. E. Shrock, E. Rockafellow, H. M. Milchberg, C. B. Schroeder, J. van Tilborg, E. Esarey, C. G. R. Geddes, and A. J. Gonsalves, Matched guiding and controlled injection in dark-current-free, 10-GeV-class, channel-guided laser-plasma accelerators, Phys. Rev. Lett. **133**, 255001 (2024).

[34] E. Esarey, C. B. Schroeder, and W. P. Leemans, Physics of laser-driven plasma-based electron accelerators, Rev. Mod. Phys. **81**, 1229 (2009).

[35] C. A. Lindstrøm, S. Corde, R. D'Arcy, S. Gessner, M. Gilljohann, M. J. Hogan, and J. Osterhoff, Beam-driven plasma-wakefield acceleration, arXiv:2504.05558.

[36] J. B. Rosenzweig, B. Breizman, T. Katsouleas, and J. J. Su, Acceleration and focusing of electrons in two-dimensional nonlinear plasma wake fields, Phys. Rev. A **44**, R6189 (1991).

[37] W. Lu, C. Huang, M. Zhou, W. B. Mori, and T. Katsouleas, Nonlinear theory for relativistic plasma wakefields in the blowout regime, Phys. Rev. Lett. **96**, 165002 (2006).

[38] See Supplemental Material at http://link.aps.org/supplemental/10.1103/ggd1-pt1y for more details about the simulations, which includes Refs. [39–42].

[39] F. Li, W. An, V. K. Decyk, X. Xu, M. J. Hogan, and W. B. Mori, A quasi-static particle-in-cell algorithm based on an azimuthal Fourier decomposition for highly efficient simulations of plasma-based acceleration: QPAD, Comput. Phys. Commun. **261**, 107784 (2021).

[40] B. Godfrey, The IPROP three-dimensional beam propagation code, Defense Technical Information Center, 1985, https://books.google.com/books?id=hos_OAAACAAJ.

[41] A. F. Lifschitz, X. Davoine, E. Lefebvre, J. Faure, C. Rechatin, and V. Malka, Particle-in-cell modelling of laser–plasma interaction using Fourier decomposition, J. Comput. Phys. **228**, 1803 (2009).

[42] D. Sagan, Bmad: A relativistic charged particle simulation library, computational accelerator physics, Nucl. Instrum. Methods Phys. Res., Sect. A **558**, 356 (2006).

[43] V. Yakimenko, L. Alsberg, E. Bong, G. Bouchard, C. Clarke, C. Emma, S. Green, C. Hast, M. J. Hogan, J. Seabury, N. Lipkowitz, B. O'Shea, D. Storey, G. White, and G. Yocky, FACET-II facility for advanced accelerator experimental tests, Phys. Rev. Accel. Beams **22**, 101301 (2019).

[44] T. K. Charles, M. J. Boland, K. Oide, and F. Zimmerman, Bunch compression and turnaround loops in the FCC-ee injector complex, J. Phys. Conf. Ser. **1067**, 062023 (2018).

[45] J. Björklund Svensson, T. K. Charles, O. Lundh, and S. Thorin, Third-order double-achromat bunch compressors for broadband beams, Phys. Rev. Accel. Beams **22**, 104401 (2019).

[46] B. E. Carlsten, K. A. Bishofberger, L. D. Duffy, C. E. Heath, Q. R. Marksteiner, D. C. Nguyen, R. D. Ryne, S. J. Russell, E. I. Simakov, and N. A. Yampolsky, New x-ray free-electron laser architecture for generating high fluxes of longitudinally coherent 50 keV photons, J. Mod. Opt. **58**, 1374 (2011).

[47] M. Tzoufras, W. Lu, F. S. Tsung, C. Huang, W. B. Mori, T. Katsouleas, J. Vieira, R. A. Fonseca, and L. O. Silva, Beam loading in the nonlinear regime of plasma-based acceleration, Phys. Rev. Lett. **101**, 145002 (2008).

[48] T. N. Dalichaouch, X. L. Xu, A. Tableman, F. Li, F. S. Tsung, and W. B. Mori, A multi-sheath model for highly nonlinear plasma wakefields, Phys. Plasmas **28**, 063103 (2021).

[49] S. Diederichs, C. Benedetti, E. Esarey, J. Osterhoff, and C. B. Schroeder, High-quality positron acceleration in beam-driven plasma accelerators, Phys. Rev. Accel. Beams **23**, 121301 (2020).

[50] S. Tomin, I. Zagorodnov, W. Decking, N. Golubeva, and M. Scholz, Accurate measurement of uncorrelated energy spread in electron beam, Phys. Rev. Accel. Beams **24**, 064201 (2021).

[51] X. Davoine, E. Lefebvre, C. Rechatin, J. Faure, and V. Malka, Cold optical injection producing monoenergetic, Multi-GeV electron bunches, Phys. Rev. Lett. **102**, 065001 (2009).

[52] A. Ferran Pousa, A. Martinez de la Ossa, and R. W. Assmann, Intrinsic energy spread and bunch length growth in plasma-based accelerators due to betatron motion, Sci. Rep. **9**, 17690 (2019).

[53] K. V. Lotov, Efficient operating mode of the plasma wakefield accelerator, Phys. Plasmas **12**, 053105 (2005).

[54] M. D. Litos, R. Ariniello, C. E. Doss, K. Hunt-Stone, and J. R. Cary, Beam emittance preservation using Gaussian density ramps in a beam-driven plasma wakefield accelerator, Phil. Trans. R. Soc. A **377**, 20180181 (2019).

[55] R. Ariniello, C. E. Doss, K. Hunt-Stone, J. R. Cary, and M. D. Litos, Transverse beam dynamics in a plasma density ramp, Phys. Rev. Accel. Beams **22**, 041304 (2019).

[56] T. C. Chiou, T. Katsouleas, C. Decker, W. B. Mori, J. S. Wurtele, G. Shvets, and J. J. Su, Laser wake-field acceleration and optical guiding in a hollow plasma channel, Phys. Plasmas **2**, 310 (1995).

[57] Y. P. Wu, J. F. Hua, C.-H. Pai, W. An, Z. Zhou, J. Zhang, S. Liu, B. Peng, Y. Fang, S. Y. Zhou, X. L. Xu, C. J. Zhang, F. Li, Z. Nie, W. Lu, W. B. Mori, and C. Joshi, Near-ideal dechirper for plasma-based electron and positron acceleration using a hollow channel plasma, Phys. Rev. Appl. **12**, 064011 (2019).

[58] P. Michel, C. B. Schroeder, B. A. Shadwick, E. Esarey, and W. P. Leemans, Radiative damping and electron beam dynamics in plasma-based accelerators, Phys. Rev. E **74**, 026501 (2006).

[59] P. Antici, A. Bacci, C. Benedetti, E. Chiadroni, M. Ferrario, A. R. Rossi, L. Lancia, M. Migliorati, A. Mostacci, L. Palumbo, and L. Serafini, Laser-driven electron beamlines generated by coupling laser-plasma sources with conventional transport systems, J. Appl. Phys. **112**, 044902 (2012).

[60] K. Floettmann, Some basic features of the beam emittance, Phys. Rev. ST Accel. Beams **6**, 034202 (2003).

[61] M. Migliorati, A. Bacci, C. Benedetti, E. Chiadroni, M. Ferrario, A. Mostacci, L. Palumbo, A. R. Rossi, L. Serafini, and P. Antici, Intrinsic normalized emittance growth in laser-driven electron accelerators, Phys. Rev. ST Accel. Beams **16**, 011302 (2013).

[62] X. L. Xu, J. F. Hua, Y P. Wu, C. J. Zhang, F. Li, Y. Wan, C.-H. Pai, W. Lu, W. An, P. Yu, M. J. Hogan, C. Joshi, and W. B. Mori, Physics of phase space matching for staging plasma and traditional accelerator components using longitudinally tailored plasma profiles, Phys. Rev. Lett. **116**, 124801 (2016).

[63] C. Lindstrøm and E. Adli, Design of general apochromatic drift-quadrupole beam lines, Phys. Rev. Accel. Beams **19**, 071002 (2016).

[64] Y. Ding, A. Brachmann, F.-J. Decker, D. Dowell, P. Emma, J. Frisch, S. Gilevich, G. Hays, P. Hering, Z. Huang, R. Iverson, H. Loos, A. Miahnahri, H.-D. Nuhn, D. Ratner, J. Turner, J. Welch, W. White, and J. Wu, Measurements and simulations of ultralow emittance and ultrashort electron beams in the linac coherent light source, Phys. Rev. Lett. **102**, 254801 (2009).

[65] P. Emma, F. Zhou, Z. Huang, and C. Behrens, Time-resolved images of coherent synchrotron radiation effects in the LCLS first bunch compressor, in *Proceedings of FEL2012, Nara, Japan* (2012), https://proceedings.jacow.org/FEL2012/papers/weoa04.pdf.

[66] G. Stupakov and J. Tang, Calculation of the wake due to radiation and space charge forces in relativistic beams, Phys. Rev. Accel. Beams **24**, 020701 (2021).

[67] M. Cornacchia and P. Emma, Transverse to longitudinal emittance exchange, Phys. Rev. ST Accel. Beams **5**, 084001 (2002).

[68] C. Mitchell, J. Qiang, and P. Emma, Longitudinal pulse shaping for the suppression of coherent synchrotron radiation-induced emittance growth, Phys. Rev. ST Accel. Beams **16**, 060703 (2013).

[69] F. Zeng, Y. Jiao, W. Liu, and C.-Y. Tsai, Cancelation of coherent synchrotron radiation kicks in chicane bunch compressors, Phys. Rev. Accel. Beams **28**, 070701 (2025).

[70] A. Martinez de la Ossa, J. Grebenyuk, T. Mehrling, L. Schaper, and J. Osterhoff, High-quality electron beams from beam-driven plasma accelerators by wakefield-induced ionization injection, Phys. Rev. Lett. **111**, 245003 (2013).

[71] L.-L. Yu, E. Esarey, C. B. Schroeder, J.-L. Vay, C. Benedetti, C. G. R. Geddes, M. Chen, and W. P. Leemans, Two-color laser-ionization injection, Phys. Rev. Lett. **112**, 125001 (2014).

[72] O. Lundh, J. Lim, C. Rechatin, L. Ammoura, A. Ben-Ismaïl, X. Davoine, G. Gallot, J.-P. Goddet, E. Lefebvre, V. Malka, and J. Faure, Few femtosecond, few kiloampere electron bunch produced by a laser–plasma accelerator, Nat. Phys. **7**, 219 (2011).

[73] R. Weingartner, S. Raith, A. Popp, S. Chou, J. Wenz, K. Khrennikov, M. Heigoldt, A. R. Maier, N. Kajumba, M. Fuchs, B. Zeitler, F. Krausz, S. Karsch, and F. Grüner, Ultralow emittance electron beams from a laser-wakefield

accelerator, Phys. Rev. ST Accel. Beams **15**, 111302 (2012).

[74] B. D. O'Shea, G. Andonian, S. K. Barber, K. L. Fitzmorris, S. Hakimi, J. Harrison, P. D. Hoang, M. J. Hogan, B. Naranjo, O. B. Williams, V. Yakimenko, and J. B. Rosenzweig, Observation of acceleration and deceleration in gigaelectron-volt-per-metre gradient dielectric wakefield accelerators, Nat. Commun. **7**, 12763 (2016).

[75] L. Serafini and M. Ferrario, Velocity bunching in photo-injectors, AIP Conf. Proc. **581**, 87 (2001).

[76] Y. Ma, D. Seipt, K. Krushelnick, and A. G. R. Thomas, Generation of straight and curved hollow plasma channels by laser-generated nonlinear wakefields and studies of ultra-intense laser pulse guiding, Phys. Plasmas **28**, 063104 (2021).